Relative spike timing in pairs of hippocampal neurons distinguishes the beginning and end of journeys

Matthew L. Shapiro* and Janina Ferbinteanu

The Fishberg Department of Neuroscience and The Alfred B. and Gudrun J. Kastor Neurobiology of Aging Laboratories, Mount Sinai School of Medicine, 1 Gustave L. Levy Place, New York, NY 10029-6574

Edited by Larry R. Squire, University of California, San Diego, CA, and approved January 10, 2006 (received for review October 4, 2005)

Episodic memory organizes experience in time, so that we can review past events and anticipate the future. In a hippocampus-dependent memory task, spike timing in pairs of simultaneously active CA1 neurons with overlapping place fields distinguished the start and end of trials. At the common starting point of different journeys, the relative spike timing of the neurons was highly correlated. As the rat approached a common goal from different starting points, however, temporal firing patterns were strongly modulated across journeys even if the cells fired in the same spatial locations within fields, implying that different processes influenced when and where cells fire. Spike timing within hippocampal ensembles may thereby help parse the beginning from the end of episodes in memory.

hippocampus | memory | neural coding

Human memory organizes experiences across time, linking events into narratives or journeys with a well defined beginning, middle, and end. People use such episodic memories to review the past and to anticipate the future (1). The hippocampus is crucial for this ability (1), and nonverbal animals may possess a similar capacity (2), defined operationally in tasks that require knowing what, when, and where (3, 4). Hippocampal neurons in behaving rats predict the animal's location by way of place fields, regions of an environment that selectively elicit high firing rates (5), but the mechanistic link between place fields and episodic-like memories remains unclear. Recent experiments have begun to better connect the neuropsychology of memory to the neurophysiology of the hippocampus. Hippocampal place fields remapped when rats performed different behaviors in the same spatial environment (6, 7) or when they performed the same overt behavior in the same location during journeys to or from different goals (8, 9). Hippocampal neurons in humans exploring a virtual reality town also fired in particular locations, typically when the subject was searching for one target among several potential goals (10). Thus, place fields in rats and people can be modulated by the goal that guides ongoing behavior.

We dissociated memory demand from spatial location and movement trajectory by training rats to go from two opposite start arms to two opposite goal arms in a plus-shaped maze (Fig. 1*a*) (11). In each trial, the rat was placed in a start arm and required to select a correct goal arm to find food; between trials, the rat was kept on a waiting platform. The start arm varied pseudorandomly, whereas the goal arm was kept the same until the rat performed reliably, then the opposite goal arm was rewarded in a new trial block. The rat thus made four types of journeys: north to east (NE), north to west (NW), south to east (SE), and south to west (SW). Because the food location alternated, the rat had to change its response to the same stimuli and remember where to find food, depending on the temporal context of the trial block. In the start arms, memory for the food location guided the prospective behavioral discrimination; in the goal arms, memory for the origin of the journey provided additional retrospective information (11). Place fields present on only one journey type (e.g., a cell firing in the north arm during NE but not NW journeys) were defined operationally as journey-dependent fields, coding either prospective (start arm) or retrospective (goal arm) information (11).

If prospective and retrospective coding reflect distinct memory functions, then their signals should differ. Because individual journey-dependent place fields did not distinguish the beginning and end of behavioral episodes (11), we investigated other aspects of hippocampal activity. Both population and temporal coding exist in the hippocampus. In spatial tasks, the time-averaged firing rate of a population as small as 60 cells predicts the location of a rat to within 1 cm (12). In principle, temporal coding may represent information not only by means of which cells fire, but also by means of when cells fire (13, 14). Indeed, hippocampal spike timing changes with respect to behavior and electroencephalogram (EEG) rhythms, and firing with respect to theta phase can predict the rat's location within a place field (15–18). We hypothesized that temporal firing patterns within ensembles of coactive neurons might differentiate the beginning from the end of journeys (Fig. 1*a*).

Results

Of 525 place fields, most were journey-dependent (11). Some of the results reported here were described previously as individual, journey-independent place fields that coded current locations (11). Here we analyzed cell pairs with overlapping journey-independent place fields that fired in reliable, theta-entrained bursts in regions of the start and goal arms selected so that movement speed, direction, and occupied spatial location were similar across journeys (Fig. 1 *a* and *b*). Any recording that failed strict behavioral and physiological criteria was excluded. Together, 52 neurons (30 in the start arm and 22 in the goal arm) recorded from three rats during 20 recording sessions formed 35 pairs of simultaneously active, overlapping place fields: 21 pairs (12 from four triplets) in the start arms and 14 pairs (6 from two triplets) in the goal arms (Figs. 5 and 6, which are published as supporting information on the PNAS web site).

Raster plots and crosscorrelations (XCRs) quantified relative spike timing between cells in a pair as rats traversed the overlapping place fields. Within a given journey, each spike of one cell of the pair (designated arbitrarily as the time-giver) was considered time 0. All spikes of the other cell occurring $\leq$200 msec before or after time 0 were separated into 20-msec bins and counted to create the XCRs (Fig. 1*c*). The $\pm$200-ms interval corresponded to approximately the time it took a rat to traverse half the length of a maze arm and included 3–4 cycles. XCRs revealed theta-frequency modulation (7.5–10 Hz) (15) (Fig. 7*a*, which is published as supporting information on the PNAS web site), and cell pairs fired with 20- to 40-msec lags in the range of the 30- to 60-Hz gamma oscillations (19) (Fig. 8*a*, which is published as supporting information on the PNAS web site). A briefer window spanned $\pm$60 msec, focused on

Conflict of interest statement: No conflicts declared.

This paper was submitted directly (Track II) to the PNAS office.

Abbreviations: ACR, autocorrelation; NE, north to east; NW, north to west; SE, south to east; SW, south to west; XCR, crosscorrelation.

*To whom correspondence should be addressed. E-mail: matthew.shapiro@mssm.edu.

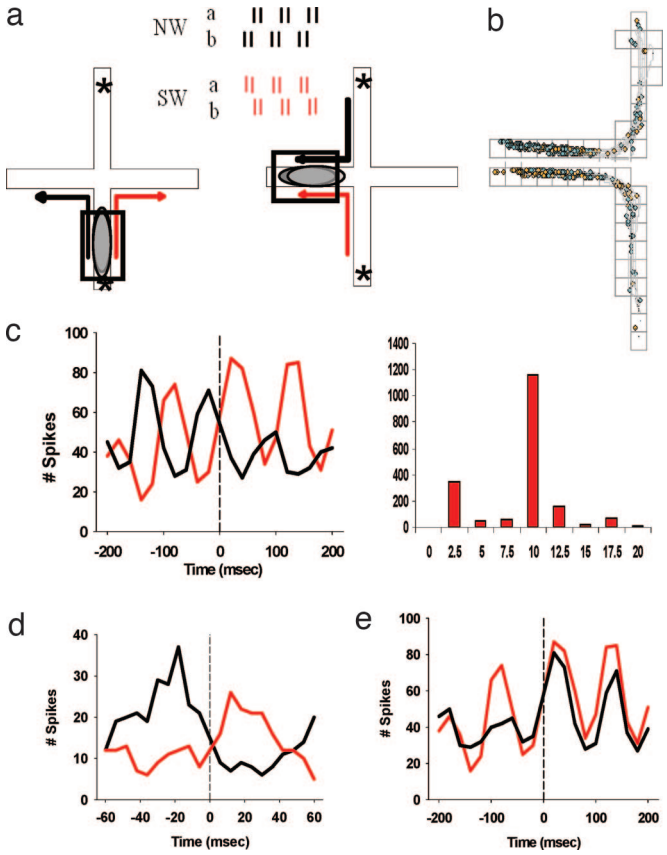

Fig. 1. Spatial and temporal firing patterns in plus-shaped maze place fields. (*a*) The rat had to walk from the north or south start arm (*) to a correct east or west goal arm. Food location switched when the animal performed reliably. Pairs of neurons analyzed here fired in overlapping, journey-independent place fields in either the start or goal arms (gray ovals). The rectangular boxes depict the spatial restrictions imposed on the data analyses. (*Inset*) A hypothetical example of across-journey change in relative temporal patterns of activity. Cell ''a'' follows cell ''b'' in NW journeys but leads in SW journeys. (*b*) Place-firing plots of two cells with overlapping place fields are shown in separate NW (*Upper*) and SW (*Lower*) journeys. (*c*) Crosscorrelation (XCR) plots (from *b*: black, NW journey; red, SW journey) summarized spike timing within a ±200-msec window. The vertical dashed line shows time 0 of the time-giver (see *Results*). (*Right*) The power spectrum of the SW XCR (prominent peak in the theta range at 10 Hz). (*d*) The same data as in *b*, which shows the XCRs in a ±120-msec window. (*e*) XCRs' time shift. The best fit between the two curves in *c* was obtained by a +260-msec time shift of the NW journey's XCR.

coupled firing within an interval ≈1 theta cycle, and verified the observations (Fig. 1*d*).

Shifts in relative spike timing across journey types were quantified by using Pearson's product moment correlation (*r*) of corresponding XCRs [e.g., for two cells with overlapping place fields in the west arm, $r(NW_{XCR}, SW_{XCR})$]. An original correlation was calculated between the two corresponding XCRs, and then the XCR of one journey was time-shifted in 20-msec increments relative to the XCR corresponding to the other journey until the two curves were best superimposed (the best time shift, Fig. 1*e*). If spike timing was unrelated to journey, then the highest correlation would be obtained in the original Pearson's *r*: a 0-msec time shift. If spike timing differed across journeys, however, then the best time shift should be nonzero. The time shifts were corrected if their direction was clearly opposite to the one calculated (i.e., a shift of +380 msec in one direction was in fact a −20-msec shift).

Relative spike timing often differed between journeys in the goal arms (Fig. 9, which is published as supporting information on the PNAS web site), but rarely in the start arms (Fig. 10, which is published as supporting information on the PNAS web site). The original correlation was higher than any shift in 16 of 21 pairs in the start arm, but only in 2 of 14 pairs in the goal arm: [$\chi^2(1) = 12.9$, $P < 0.0003$]. In the start arm, the XCRs' correlations were high, and the best time shifts were low; in the goal arm the XCRs' correlations were relatively low, and the best time shifts were markedly and significantly higher than zero (Fig. 2*a*). The lowest correlations in the goal arm corresponded to the most different XCRs and predicted the XCR time shifts: [$F_{(1,12)} = 5.02$, $P = 0.04$]. In most cases, firing lag between cells was the same across journeys in the start arm but different in the goal arm (Fig. 8*b*), where, in some cases, firing order reversed so that a cell that lagged in one type of journey led in the other (Fig. 9). Spike timing thereby may convey information as the animal approaches the end of the journey.

To assess whether common inputs and intrinsic excitability produced synchronous firing in cell pairs (20), Monte Carlo simulations randomized the spike sequences, and the XCRs were recalculated. These shuffled XCRs should continue to show oscillations corresponding to inter- and intraburst interspike intervals (21) but not systematic sequential firing between cells (22). Indeed, shuffled XCRs were theta-frequency modulated (Fig. 7*b*), and, in the start arms, typically had the same 0-time shifts as the original XCRs. In the goal arms, however, the shuffled XCRs' time shifts were significantly lower than the actual ones (Fig. 2*b*). Thus, synchronous firing timed by intrinsic oscillations did not explain XCR time shifts.

Three other factors may have varied systematically with journeys to change relative spike timing in the goal arm. One or both of the cells in a pair may have fired with different intrinsic rhythms or spatial patterns, or spatial behavior may have been less stereotyped in the goal than in the start arms.

If altered relative spike timing was driven by individual cells firing with different rhythms across journeys, then autocorrelations (ACRs) should change systematically between journeys and predict XCR time shifts. But the ACRs were similar between journeys with time shifts ≈0, did not differ between arms (Fig. 3*a*), and did not predict XCR time shifts in either arm (Fig. 3*b*). Thus, pairs of cells in the goal arms fired in reliable temporal patterns individually yet with different relative spike-timing patterns between journeys.

If changes in relative spike timing were caused by altered spatial firing patterns, then such variations should predict time shifts in XCRs. Although firing rates within place fields differed slightly between journeys, the difference did not distinguish the start from the goal arms and was unrelated to the XCR time shifts (Fig. 4*a*). Place fields of individual cells varied more in the goal than in the start arms between journeys (Fig. 4*b* and, for examples, Figs. 9–12, which are published as supporting information on the PNAS web site) but spatial correlations did not predict the XCR time shifts (Fig. 4*c*). Neither place field centers, centroids, size, location of spiking onset of single cells, nor relative shift in the location of spiking onset in pairs explained the XCR time shift in the goal arm (Figs. 13–15 and Table 1, which are published as supporting information on the PNAS web site). Thus, altered spike timing at the end of different journeys was not caused by altered spatial firing.

Spatial behavior, although consistent across journeys, could have been less stereotyped in the goal than the start arms and thus could have influenced relative spike timing. If so, then behavioral parameters should be more variable in the goal than the start arm and predict the XCR time shifts between journeys. In fact, spatial behavior was significantly more homogenous in the goal than in the start arms [ANOVA start vs. goal arm journey correlations, $F_{(1,50)} > 32$, $P < 0.001$; visits, $F_{(1,50)} = 1.05$, $P = 0.31$] across all grid sizes and in all measures (except the visit correlations, which did not differ statistically). None of the behavioral measures predicted the XCR time shifts in either arm (Table 1).

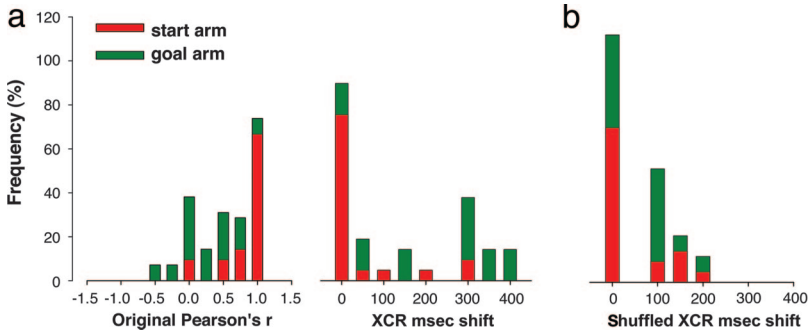

Fig. 2. XCRs obtained from different journeys were similar in the start arms but not the goal arms. (*a*) The histograms show the distributions of the XCRs' original correlations (*Left*) and the XCRs' time shift (*Right*). Across journeys, XCRs were highly similar in the start arm (mean $r = 0.76$) but varied widely in the goal arm [mean $r = 0.17$; different from start, $t(33) = 4.56$, $P = 0.0001$]. Correspondingly, the XCR time shifts were low in the start arm [mean = 39.4 msec; median = 0 msec; mode = 0 msec; different from 0, $t(20) = 1.96$, $P = 0.06$] and high in the goal arm [mean = 162.8 msec; median = 120 msec; mode = 300 msec; different from 0, $t(13) = 4.2$, $P = 0.001$; different from start, Kolmogorov–Smirnov two-sample maximum difference test = 0.62, $P = 0.002$]. (*b*) Shuffling the spike trains by using Monte Carlo simulations and recomputing the XCRs did not markedly alter the XCRs' time shifts in the start arm (Wilcoxon rank test = −1.105, $P = 0.917$) but significantly reduced the journey-related time shifts in the goal arm (Wilcoxon rank test = −2.714, $P = 0.007$).

Discussion

The neural codes for different episodes that end in the same place were more distinct than codes for different episodes that began in the same place, suggesting that the hippocampus distinguishes the start and end of journeys. Together with population coding (11), spike timing conveys distinctions both between start and goal arms and between different journeys to the goal arm and does so because spike timing varies with different behavioral histories.

What mechanisms could produce this distinction? The past experience of the animal was more distinct in the goal than in the start arms, where each journey was preceded by time on the waiting platform. In the goal arm, the start of the journey, recent spatial trajectory, visual input, and body turn differed between trials. If hippocampal activity reflects recent history, then the more distinct events preceding goal entry may have contributed to the XCR time shift at the end of the journeys. By contrast, such variables as the pending reward were identical between journeys and thus could not contribute to XCR differences.

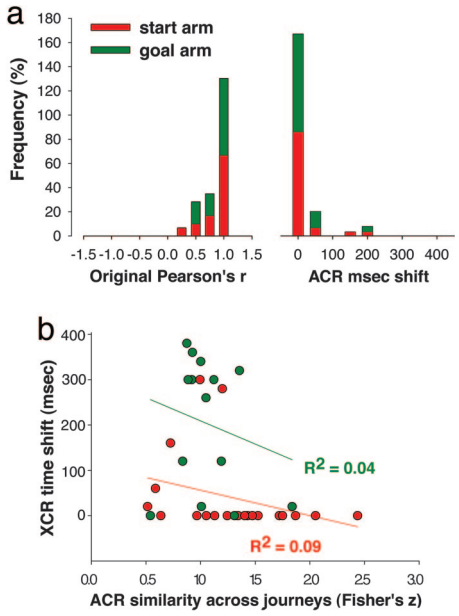

Fig. 3. ACRs were similar between journeys and did not show time shifts. (*a*) The histograms show the distributions of ACRs' original correlations (*Left*) and the ACRs' time shifts (*Right*). In both start and goal arm, the ACRs of single cells were similar across journeys [mean Fisher's z from Pearson's r, start = 1.18; goal = 1.07; $t(50) = 0.71$, $P = 0.47$], did not show time shifts different from 0 [(start: $t(29) = 1.56$, $P = 0.12$] [goal: $t(21) = 1.30$, $P = 0.2$], and did not differ between arms (Kolmogorov–Smirnov test = 0.05, $P = 1.0$). (*b*) ACRs' similarity between journeys did not predict XCR time shifts in either the start [red, $F_{(1,19)} = 1.93$, $P = 0.18$] or in the goal arm (green, $F_{(1,12)} = 0.55$, $P = 0.46$). The horizontal axis shows the mean ACRs' correlation calculated between the two cells corresponding to a given XCR (data transformed to Fisher's z). The vertical axis shows XCRs' time shifts in msec.

The temporal structure of hippocampal unit activity encodes information beyond a rate code for place. Although the rate and firing sequence of hippocampal pyramidal neurons are correlated when rats traverse a linear track in stereotyped trajectories (23), if the track is shortened, place fields shrink and the firing rate declines, although the firing phase continues to vary with the animal's location within a field (16). Here cell pairs also fired in theta-frequency oscillations, but theta frequency-entrained bursting was not sufficient to account for the XCR time shifts at the end of journeys. Rather, the change in relative spike timing likely occurred through a change in the mean theta phases of the two cells (15–18), although this possibility was not tested directly. Spike timing in hippocampal neurons is predicted by the activity of other neurons active 10–30 msec earlier and is not fully dependent on the theta rhythm (15). This interval corresponds well with the 20- to 40-msec lag separating the activity of cells with overlapping place fields described here, where firing sequence, spatial distribution, and rate varied independently, whereas spatial behavior was kept constant, and behavioral history differed. Such timing changes may reflect the intrinsic organization of hippocampal network activity and reveal memory coding (15).

If the distinct behavioral trajectories preceding entries into the goal arm altered spatial firing patterns systematically, then the relative theta phase of spiking in cell pairs could change and thus modulate spike timing (16, 18). Because no measure of spatial firing predicted changes in relative spike timing, however, other mechanisms likely influence the journey-related firing patterns in the goal arm. Different population or temporal input patterns from the entorhinal cortex (9, 24) or the hippocampus (11) or recurrent activity within the CA3 network (25, 26) could alter timing sequences among CA1 cell firing even as theta modulation of activity is maintained.

Hippocampal cells with classical place fields are proposed to encode either locations (5) or the commonalities among events (27). We reported previously that the hippocampus signaled temporally extended representations of journeys in which both the beginning and the end of different episodes were signaled through distinct population codes (11). Here we found that only at the end of a journey did spike timing in ensembles of "place" cells become journey-specific, so that similar behaviors with distinct histories were distinguished through temporal as well as population codes (Fig. 16, which is published as supporting information on the PNAS web site). Thus, relative spike timing in overlapping place fields suggests three previously unreported memory signals beyond those generated by journey-dependent place fields: (*i*) an additional retrospective signal in the goal arm that is not found in the start arm,

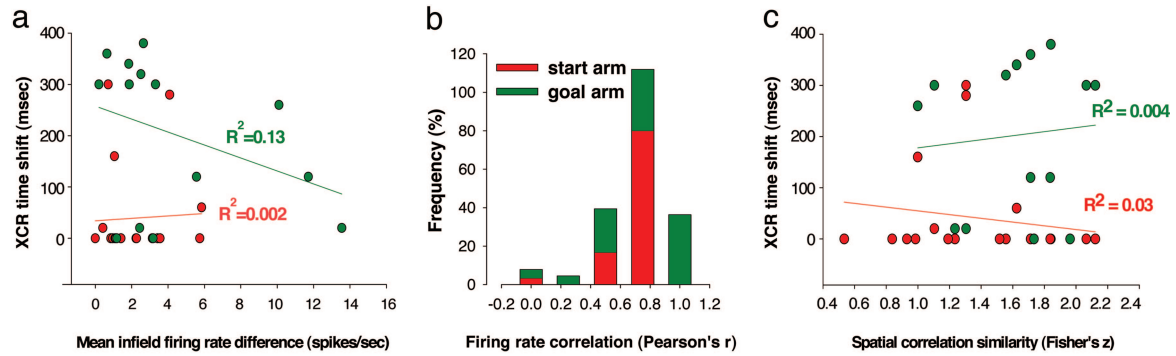

Fig. 4. Temporal firing patterns and spatial characteristics of place fields were unrelated (red, start arm; green, goal arm). (*a*) Variations across journeys in mean firing rates within place fields (horizontal axis, start arm = 2.27 spikes per sec; goal arm = 3.96 spikes per sec) were reliably >0 [start: $t(29) = 6.93$, $P < 0.001$] [goal: $t(21) = 3.95$, $P < 0.01$] but did not distinguish the beginning from the end of journeys [$t(50) = 1.80$, $P = 0.07$) and did not reliably predict the time shift of the XCRs [vertical axis: start, $F_{(1,19)} = 0.038$, $P = 0.84$; goal, $F_{(1,12)} = 1.87$, $P = 0.19$]. Each point on the horizontal axis represents the mean calculated between the two cells corresponding to a given XCR. (*b*) Between journeys, the spatial distribution of firing rates varied more in the goal arm [$F_{(1,50)} = 43.2$, $P < 0.001$). (*c*) Relative spike timing and infield firing rate distributions did not covary in either arm [start: $F_{(1,19)} = 0.76$, $P = 0.39$] [goal: $F_{(1,12)} = 1.65$, $P = 0.22$]. Each point on the horizontal axis represents the mean correlation of firing-rate distributions calculated between the two cells corresponding to a given XCR. The vertical axis shows XCR time shifts.

(*ii*) a signal that the end of a journey is imminent, and (*iii*) an increased distinctiveness of memory representations as behavior progressed from appetitive anticipation of expected events to just before consummatory behavior, when a goal was attained and the episode belonged to the past (Fig. 17, which is published as supporting information on the PNAS web site).

Together, the population and temporal coding reflected the structure of a hippocampus-dependent task with episodic-like aspects (3) by forming a temporally extended and asymmetric representation. Although our experiment equated start and goal arms with the beginning and end of episodes and our descriptions emphasized these extremes, the coding of behavioral history in memory may be continuous rather than dichotomous, and spike timing may reflect this continuity. From this view, the start of different journeys to similar goals should be coded by correlated network activity patterns, whereas the approaching end of different journeys to the same goal should reflect increasing "pattern separation" that allows the distinct coding of episodes. Future experiments are necessary to determine if hippocampal neurons reflect the unfolding history of events even when overt behavior does not dissociate different episodes (28).

Materials and Methods

Subjects. Five male Long–Evans rats, 400–600 g, 4–6 months old (Charles River Breeding Laboratories), were housed singly (12:12 h light cycle), trained in the plus-shaped maze task, and implanted with recording electrodes (11).

Apparatus. The plus-shaped maze was made of wood, painted gray, and elevated 81.3 cm from the floor of a room that contained several visual cues, including computer racks, chairs, a bulletin board, posters, a window covered with a white blind, and two standing lamps located in the NE and NW corners. Each of four arms was 59.7 cm long and 6.4 cm wide. Two opposing arms were designated as goal arms; the other arms were designated as start arms. A gray wooden block, 29.2 cm high, 6.2 cm wide, and 22 cm deep, barred the start arm, which was unused during a trial. An octagonal waiting platform, 16.5 cm per side and painted black, was next to the maze.

Behavioral Training and Testing. The north and south arms of the maze were designated as start arms; the west and east arms were designated as goal arms. At the start of each trial, half of a Froot Loop (Kellogg, Battle Creek, MI) was put at the end of one goal arm, the wood block was put into the unused start arm, and the rat was placed at the distal end of the other start arm, facing the choice point. Each rat was trained to walk to the food and was allowed to self-correct if it first entered the wrong arm. The start arm was selected from a pseudorandom sequence of 60 trials with ≤3 consecutive repetitions. The alternating start arm sequence was intended to discourage the rat from using a body-turn strategy to find the food (29, 30). After the rat reached the goal and ate the Froot Loop, it was placed on the waiting platform for 10–15 sec while the correct arm was baited and the block was put in the appropriate start arm. After the rat entered the correct goal arm in 9 of 10 consecutive trials, the other goal arm was baited and a new block of trials began. The start of each new block was signaled; the rat was put into the correct goal arm, where it ate half of a Froot Loop. Alternating blocks continued throughout each daily session and included as many as 60 trials. Rats were trained to a criterion of 70–80% correct, implanted with recording electrodes, and trained to 90% correct after surgery.

Electrodes and Surgery. Each rat was tranquilized with 0.1 mg of xylazine and 0.02 mg of acepromazine, i.p., anaesthetized with isoflurane, and placed in a stereotaxic apparatus. Twelve tetrodes (31) made from four twisted wires (Ni–Cr wire, Rediohm-800, 12.7 μm, Kanthal, Palm Coast, FL) and two reference wires were loaded into a 14-drive assembly (Neuro-Hyperdrive; Kopf Instruments, Tujunga, CA), which allowed independent vertical movement of each drive. The electrode assembly was mounted on the skull with dental cement and bone screws that connected ground wires. The tip of the assembly was lowered to the cortical surface (anteroposterior −3.8 mm, mediolateral −2 mm from bregma). At the end of surgery, the tetrodes were driven 1.25 mm into the brain. Testing resumed 1 week after surgery.

Recording Methods. The hyperdrive assembly was mated to a 6-cm-diameter headstage with 54 unity gain amplifiers and 10 color light-emitting diodes for position tracking. Unit signals were differentially amplified (×1,000–5,000), filtered (600–6,000 Hz), digitized (32 points per waveform, 1-msec sample, and 1 μsec of resolution), and stored with light-emitting diode positions by computer (CHEETAH 64 Data Acquisition System, Neuralynx, Tucson, AZ). Waveforms were displayed on a computer screen and played through two audio speakers while the rat was on the hexagonal platform. System noise was <30 μV. When stable and isolable complex spike (CS) units were found (32–34), a recording session ensued that lasted as long as 90 min. Otherwise, the electrodes were advanced 20–30 μm, and at least 4 h elapsed before recording to

allow the brain tissue to stabilize. Units with spike amplitudes >100 μV and at least twice the mean noise were discriminated off-line by identifying clusters defined by waveform parameters (Fig. 6): One to 15 waveforms were separated per tetrode. Because the tetrodes may have shifted overnight, even when they were not advanced at the end of the recording session, every distinct and isolated waveform was operationally defined as a different unit. Because cells were recorded extracellularly, the same neurons may have generated different waveforms over days, so the precise number of recorded neurons cannot be known definitively (35). Behavioral measures of speed, distance, and direction of movement were calculated from the tracked position of the color light-emitting diodes.

Data Analysis. ***Place field definition and statistics.*** The light-emitting diode positions (640 × 480 camera pixels, 0.77 cm per pixel, and 16.7 msec per sample) were smoothed by using a moving boxcar average of 5–10 sequentially collected points that occurred within a maximum of 1 sec and 10–20 camera pixels of one another. To define place fields, the maze arena was divided into a 28 × 28 array of 7 × 7 cm grid units. Varying the array size between 16^2 (12.3 cm) and 64^2 (3.0 cm) grid units showed similar patterns of results (see description of spatial behavior below). Firing rate was calculated by dividing the total number of spikes by the total amount of time spent in each grid unit. Place activity was analyzed if the grid unit was visited for a total visit duration of ≥300 msec and ≥5 times. Firing rates were calculated only if the rat was moving >2 cm/sec. For each cell, a place field was defined as an area ≥2 adjacent grid units, with the mean firing rate >1 spike per sec with ≥5 spikes per subfield visit. Noncontiguous patches with firing above threshold were defined as "subfields." If a cell had a place field on more than one arm, it was treated as having individual subfields on each relevant arm, or, if the place field extended in the choice point area, the analysis included only spikes fired outside of that area.

Place field size was calculated by summing the number of pixels that were included in the field. Final analyses included fields on average 6.8 ± −2.15 grid units in size. Place field centers (mean x and y coordinates of the field) and centroids ("center of mass") were calculated by weighting each grid unit in the field by its firing rate r so that centroid $x = \Sigma(x_i r_i)/\Sigma r$ and $y = \Sigma(y_i r_i)/\Sigma r$.

Trial separation and journey analyses. Event flags generated on-line categorized maze locations (e.g., start of north arm, maze center, end of west arm), marked the beginning and end of each trial, and signaled the entry into the correct goal arm or an error. The flags identified and were used to sort each trial into one of five subfiles containing only one of the four journey types (e.g., NE, SW, etc.) or error trials (when the rat first entered the wrong goal arm). To compare journeys, the entire recording session was sorted into these five subfiles. Each place field was assessed in the two types of journeys that included the arm with the field (Fig. 1*b*). To assess the influence of individual journeys, including error trials, on firing, each trial from every recording session was replayed off-line and visually inspected. This method ensured that each subfile contained only one type of journey in which the animal ran well. In 201 of 525 cases, the field was present in both corresponding journeys, and it was defined as journey-independent; only these cells are discussed here. Only journey pairs with similar movement direction, running speed, and position were retained for subsequent place field analyses.

Spatial behavior was quantified by calculating the visit locations, movement speed, and direction of movement in each of the eight cardinal compass point headings for each subfile containing one journey type. Each maze arm was represented by a 2 × 5 (start arm) or 2 × 6 (goal arm) array of grid units (7 × 7 cm per grid unit). The start arm array was shorter than the goal arm array by one grid unit to account for the rat's starting orientation facing the choice point in the start arm. Each measure of spatial behavior was calculated for every grid unit so that one array described the spatial distribution of 1 parameter across the length and width of each arm with a resolution that approximated the size of the rats' headstage. The array included the length (≈40 cm) of each arm but excluded the area of the choice point (≈20 cm), where body turns occurred, and the food cup area, where behavior changed markedly. The array divided the 6.4-cm width of each arm in two and included regions where the rat's head could extend past the edge of the arm. Paired t tests assessed whether spatial behavior was equivalent in each pair of corresponding journeys. For example, the north-arm visit array during NE trials was compared with the corresponding array for NW trials. A significant difference ($P < 0.05$) in any of the behavioral measures (visit locations, movement speed, or direction of movement) excluded the associated place fields from further consideration. Replaying every journey showed this quantification was conservative, and the trajectory plots show the similarity of spatial trajectories between journeys (Fig. 5). Trajectory similarities were compared by using spatial correlations. The maze was divided into 16, 24, 28, 32, 48, or 64 grid units (12.3, 7.0, 6.2, 4.1, 3.1, or 1.5 cm on a side), and between-journey correlations in visit location, running speed, dwell time, and movement direction were compared in the restricted zones of the start and goal arms.

Spike pairs. Additional selection filters for each spike pair required that (*i*) each place field fired at least 100 spikes in 10 journeys (i.e., reliable activity) and showed clear theta frequency modulation visible in ACR plots (Fig. 7*a*), and (*ii*) each journey-independent unit had to have at least one counterpart recorded in the same session, active in the same location, and meeting the criteria described earlier. Fifteen of the cell pairs had distinct waveforms recorded from the same tetrode; the remaining 20 pairs were recorded from different tetrodes, and no differences between these sets or among different rats were observed (Fig. 5*c*). Eighteen of the 35 cell pairs were derived from triplets of neurons with overlapping fields (four sets in the start arm and two sets in the goal arm). Each of these triplets was analyzed as three independent pairs.

The location of the onset of activity for each unit was computed for each journey. After the data were parsed into individual trials and filtered to exclude regions near the choice point (±20 cm from the center of the maze) and the food cup (Fig. 1), the position of the first spike of the unit in the arm with the place field was recorded. For example, if a pair of journey-independent cells had a place field on the south arm, the SE and SW files of that recording session were divided into individual trials. For each cell, the position of the first spike that occurred within the restricted zone of the south arm was extracted for each trial. The mean of these locations across the trials constituting a specific type of journey defined the firing onset position for that unit. The geometric distance between firing onset positions between journeys was computed for each cell, and regression analyses investigated if the variance in timing activity patterns between journeys in either the start or the goal arm was explained by either the firing-onset locations of individual cells or the relative shift of the onset locations per pairs of cells.

Temporal analyses. Raster plots were used to illustrate relative spike timing in cell pairs as rats traversed overlapping place fields. The plots were computed by assigning one member of each pair of cells to be a time-giver. Each spike of the time-giver established the center (time 0) of one horizontal raster line (e.g., the vertical lines in Figs. 9 *b* and *c* and 10 *b* and *c*) spanning the duration of interest (e.g., ±200 msec), and every spike of the other member of the cell pair occurring within that interval was plotted along that line; the distance from time 0 along the line to a given spike of the other cell corresponds to the interval between the spikes. The second spike of the time-giver established time 0 for the second raster line, and so on. Thus, the number of rows in a raster was determined by the number of spikes fired by the time-giver cell within the spatial region, including the place field. The ±200-ms interval approximated the time required to traverse half the length of a maze arm and included 3–4 cycles in the theta frequency range (7.5–10 Hz). The raster plots were normalized to a fixed height by scaling the

number of time-giver spikes to the window screen coordinates. This scaling was used only for the plots, not for statistical analyses. The temporal pattern of activity for single cells (ACRs) was displayed by using a procedure identical to the one described for XCRs (see below) but by plotting a raster showing the interspike intervals of the cell timed against itself rather than against its pair.

XCRs were computed by dividing the raster duration into bins of equal interval (e.g., ±200 msec into 20 20-msec bins) and summing the spikes that occurred in each bin across all rows (Fig. 1*c*). To ensure that the observed patterns represented the actual temporal variation of firing rather than an artifact imposed by binning, we varied the duration of interest as well as the number and width of the bins. ACRs were computed similarly. The interval between time 0 and the nearest peak of an XCR characterized the first-order interspike interval of a given cell pair for a given journey; this defined the peak lag (Fig. 8*a*). The difference in spike order between journeys was characterized by differences in peak lags (lag shift; Fig. 8*b*). Because overall XCR magnitude depended on sampling and firing rate and therefore could be artificially influenced by varying trial numbers, we normalized the XCRs by dividing each bin by the number of trials that comprised a given type of journey. Thus, if a rat made 10 NE journeys and 12 NW journeys, each bin in the NE XCR was divided by 10, and each bin in the NW XCR was divided by 12. Normalization only affected the magnitude of the XCR and had no effect on temporal pattern of activity. We used regular *t* tests and ANOVAs for all statistical analyses. Additionally, nonparametric tests were used when there was an indication that the data may not have been normally distributed.

Time-shifted XCRs. The similarity between two XCRs from corresponding journeys was calculated by using Pearson's *r*. Thus, if two cells had overlapping fields on the north arm, then the two XCRs, one for the NE and one for the NW journeys, were compared by using Pearson's product moment correlation coefficient, the original Pearson's *r*. If the firing pattern was similar in the NE and NW journeys, then the original Pearson's *r* should approach 1 (e.g., Fig. 2*a*). A time-shifted Pearson's *r* then assessed the best temporal fit between the XCRs derived from the different journeys. The XCR from one journey (e.g., NE in the example above) was shifted systematically one bin at a time, relative to the XCR from the other journey (e.g., NW), and a second time-shifted Pearson's *r* was recalculated for each shift. The highest time-shifted Pearson's *r* indicated the point where the two XCRs were most similar (the best time shift; Fig. 1*e*). The time shift between journeys was quantified by multiplying the numbers of bins by the bin size in msec (20 msec). Corrections were introduced where the real shift of the two XCRs was in the opposite direction of the one actually computed (e.g., a 380-msec shift was in fact a 20-msec shift). To ensure that the observed changes were not due to binning artifacts, we varied the bin numbers and durations (± 8, 10, 16, and 20 bins, corresponding to bin widths of 3–25 msec), and the same pattern of results were obtained. All statistical tests using Pearson's *r* values were done by using Fisher's *z* transformation. A similar procedure was applied to ACRs.

Shuffled XCRs. To verify that the observed XCRs and ACRs were different from that expected by the random coincidence of action potentials, we compared actual XCRs to the distribution of spiking expected from random activity at the mean firing rate. The interspike intervals of the cell other than the time-giver were shuffled by raster according to a time-seeded random number generator. Note that, although the order of these spikes was altered, the spatial locations of these spikes were still restricted to the arm areas as described above. In a Monte Carlo simulation, the shuffling procedure was performed 1,000 times on the same data, generating 1,000 correlograms that were then averaged to generate the final shuffled XCR or ACR (21). The shuffled XCRs maintained some rhythmicity in the theta frequency range (Fig. 7*b*). If the shuffled XCR peaks were inverted in one journey compared with the other, so that a valley occurred at time 0 in one journey, and a peak occurred there in the other, the average difference between the peaks closest to time 0 was used to calculate temporal shifts.

Power spectra. To assess the degree to which the actual and shuffled XCRs and ACRs reflected oscillations in the theta range, each 400-msec correlogram was analyzed by using fast Fourier transforms (FFTs, Systat, Richmond, CA). Because FFTs require a series length of 2^n, 16-bin correlograms were computed. To normalize the curves around 0 (analogous to removing direct current offset), the series mean was subtracted from each bin; to remove artifactual frequencies introduced by edge discontinuities, each XCR or ACR was tapered to 0 (split cosine bell) at the ends. The resulting nine-bin periodogram described the power of frequencies between 2.5 and 20 Hz in 2.5-Hz increments (Fig. 1*c Inset*). For each correlogram, theta was quantified as the proportion of power in the 5- to 12-Hz range: $\Sigma^{6}_{\text{bin}=3}$ power/$\Sigma^{9}_{\text{bin}=1}$ power. If all power was in bins 3–6 (5–12 Hz), then the proportion of theta would be 1.0; if the power were distributed equally among all nine bins, then the proportion of theta would be 0.44 (4/9).

Histology. Each rat was overdosed with pentobarbital (100 mg/kg, i.p.) and perfused transcardially with normal saline/10% formalin, and coronal brain sections (40 μm) were stained with formol/thionin to highlight cell layers and fiber tracts. Electrode tracks traversed the CA1 and CA3 layers.

We thank Sean Wright, Pam Kennedy, Amir Bahar, and Erin Rich for helpful comments; Ben Schneider for technical work; Alex Casti for analytic advice; and Anna Balk for programming. This work was supported by National Institutes of Health Grants MH65658 and DA14166 and the Mount Sinai School of Medicine.

1. Tulving, E. & Markowitsch, H. J. (1998) *Hippocampus* **8,** 198–204.
2. Morris, R. G. (2001) *Philos. Trans. R. Soc. London B* **356,** 1453–1465.
3. Clayton, N. S., Griffiths, D. P., Emery, N. J. & Dickinson, A. (2001) *Philos. Trans. R. Soc. London B* **356,** 1483–1491.
4. Clayton, N. S. & Dickinson, A. (1998) *Nature* **395,** 272–274.
5. O'Keefe, J. & Dostrovsky, J. (1971) *Brain Res.* **34,** 171–175.
6. Markus, E. J., Qin, Y. L., Leonard, B., Skaggs, W. E., McNaughton, B. L. & Barnes, C. A. (1995) *J. Neurosci.* **15,** 7079–7094.
7. Wiener, S. I., Paul, C. A. & Eichenbaum, H. (1989) *J. Neurosci.* **9,** 2737–2763.
8. Wood, E. R., Dudchenko, P. A., Robitsek, R. J. & Eichenbaum, H. (2000) *Neuron* **27,** 623–633.
9. Frank, L. M., Brown, E. N. & Wilson, M. (2000) *Neuron* **27,** 169–178.
10. Ekstrom, A. D., Kahana, M. J., Caplan, J. B., Fields, T. A., Isham, E. A., Newman, E. L. & Fried, I. (2003) *Nature* **425,** 184–188.
11. Ferbinteanu, J. & Shapiro, M. L. (2003) *Neuron* **40,** 1227–1239.
12. Wilson, M. A. & McNaughton, B. L. (1993) *Science* **261,** 1055–1058.
13. Hebb, D. O. (1949) *The Organization of Behavior* (Wiley, New York).
14. Singer, W. (1999) *Neuron* **24,** 49–65.
15. Harris, K. D., Csicsvari, J., Hirase, H., Dragoi, G. & Buzsaki, G. (2003) *Nature* **424,** 552–556.
16. Huxter, J., Burgess, N. & O'Keefe, J. (2003) *Nature* **425,** 828–832.
17. Mehta, M. R., Barnes, C. A. & McNaughton, B. L. (1997) *Proc. Natl. Acad. Sci. USA* **94,** 8918–8921.
18. O'Keefe, J. & Recce, M. L. (1993) *Hippocampus* **3,** 317–330.
19. Penttonen, M., Kamondi, A., Acsady, L. & Buzsaki, G. (1998) *Eur. J. Neurosci.* **10,** 718–728.
20. Perkel, D. H., Gerstein, G. L. & Moore, G. P. (1967) *Biophys. J.* **7,** 419–440.
21. Aertsen, A. M. H. J., Gerstein, G. L., Habib, M. K. & Palm, G. (1989) *J. Neurophysiol.* **61,** 900–917.
22. Abeles, M. & Gerstein, G. L. (1988) *J. Neurophysiol.* **60,** 909–924.
23. Mehta, M. R., Lee, A. K. & Wilson, M. A. (2002) *Nature* **417,** 741–746.
24. Buzsaki, G. (2002) *Neuron* **33,** 325–340.
25. Jensen, O. & Lisman, J. E. (2005) *Trends Neurosci.* **28,** 67–72.
26. Lisman, J. E. & Otmakhova, N. A. (2001) *Hippocampus* **11,** 551–568.
27. Eichenbaum, H., Dudchenko, P., Wood, E., Shapiro, M. & Tanila, H. (1999) *Neuron* **23,** 209–226.
28. Kennedy, P. J. & Shapiro, M. L. (2004) *J. Neurosci.* **24,** 6979–6985.
29. Packard, M. G. & McGaugh, J. L. (1996) *Neurobiol. Learn. Mem.* **65,** 65–72.
30. Restle, F. (1957) *Psychol. Rev.* **64,** 217–228.
31. Gray, C. M., Maldonado, P. E., Wilson, M. & McNaughton, B. (1995) *J. Neurosci. Methods* **63,** 43–54.
32. Ranck, J. B., Jr., Kubie, J. L., Fox, S. E., Wolfson, S. & Muller, R. U. (1982) in *Behavioral Contributions to Brain Research*, ed. Robinson, T. E. (Oxford Univ. Press, New York).
33. Fox, S. E. & Ranck, J. B. (1981) *Exp. Brain Res.* **41,** 399–410.
34. O'Keefe, J. (1979) *Prog. Neurobiol.* **13,** 419–439.
35. Knierim, J. J. (2002) *J. Neurosci.* **22,** 6254–6264.